NANO LETTERS

Letter

pubs.acs.org/NanoLett

Terms of Use CC-BY

Observing Graphene Grow: Catalyst–Graphene Interactions during Scalable Graphene Growth on Polycrystalline Copper

Piran R. Kidambi,[†] Bernhard C. Bayer,[†] Raoul Blume,[‡] Zhu-Jun Wang,[§] Carsten Baehtz,[∥] Robert S. Weatherup,[†] Marc-Georg Willinger,[§] Robert Schloegl,[§] and Stephan Hofmann*,[†]

[†]Department of Engineering, University of Cambridge, Cambridge CB3 0FA, United Kingdom

[‡]Helmholtz-Zentrum Berlin für Materialien und Energie, D-12489 Berlin, Germany

[§]Fritz-Haber-Institut der Max-Planck-Gesellschaft, D-14195 Berlin-Dahlem, Germany

[∥]Institute of Ion Beam Physics and Materials Research, Helmholtz-Zentrum Dresden-Rossendorf, D-01314 Dresden, Germany

Supporting Information

ABSTRACT: Complementary in situ X-ray photoelectron spectroscopy (XPS), X-ray diffractometry, and environmental scanning electron microscopy are used to fingerprint the entire graphene chemical vapor deposition process on technologically important polycrystalline Cu catalysts to address the current lack of understanding of the underlying fundamental growth mechanisms and catalyst interactions. Graphene forms directly on metallic Cu during the high-temperature hydrocarbon exposure, whereby an upshift in the binding energies of the corresponding C1s XPS core level signatures is indicative of coupling between the Cu catalyst and the growing graphene. Minor carbon uptake into Cu can under certain conditions manifest itself as carbon precipitation upon cooling. Postgrowth, ambient air exposure even at room temperature decouples the graphene from Cu by (reversible) oxygen intercalation. The importance of these dynamic interactions is discussed for graphene growth, processing, and device integration.

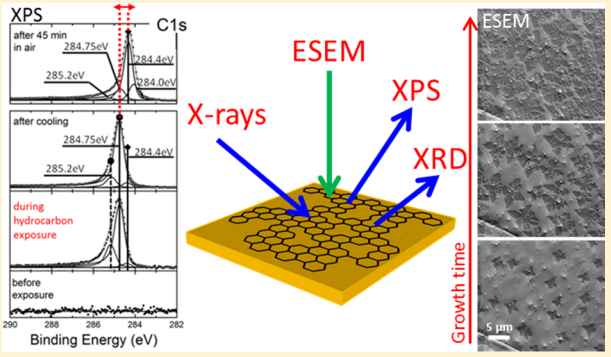

KEYWORDS: *Graphene, chemical vapor deposition (CVD), polycrystalline copper (Cu), in situ X-ray photoelectron spectroscopy, in situ X-ray diffractometry, environmental scanning electron microscopy, intercalation*

The route toward the commercial exploitation of graphene's unique properties hinges entirely on the development of adequate graphene growth and integration technologies. Chemical vapor deposition (CVD) using hydrocarbon precursors over commercially available polycrystalline Cu foil catalysts is the most widely used process to date to achieve continuous, high-quality monolayer graphene (MLG) over large areas.[1,2] Cu offers a rather error-tolerant window for the formation of MLG.[3] This has been commonly attributed to the low carbon solubility of Cu on the basis of which an isothermal, surface-based mechanism of graphene formation has been suggested.[4−7] However, the detailed growth mechanisms and interactions of the inherently polycrystalline graphene with the Cu substrate during CVD remain largely unexplored, especially for scalable CVD conditions and polycrystalline Cu. Recent reports on mismatch epitaxy[8−13] suggest that, while the graphene lattice is incommensurate on any of the Cu surfaces, there are process-dependent relationships between the Cu surface and MLG domain shape and orientation. The key missing link to understand these relations is how Cu interacts with the growing graphene and how this graphene–Cu interaction evolves postgrowth, for example, after ambient air exposure. The latter also affects subsequent MLG transfer,[14] Cu corrosion under MLG,[15−19] and an increasing number of applications that utilize or contact graphene directly on the catalyst metal.[20−25]

To determine the nature of this MLG–Cu interaction during and after growth, we fingerprint the entire graphene CVD process on polycrystalline Cu in situ, under actual reaction conditions. Using realistic hydrocarbon exposures up to mbar pressure levels, we employ complementary time- and process-resolved in situ X-ray photoelectron spectroscopy (XPS), in situ X-ray diffractometry (XRD), and environmental scanning electron microscopy (ESEM). We find the Cu catalyst surface and bulk to be in the metallic state during CVD, but the C1s XPS core level signatures for isothermally growing MLG to be shifted to higher binding energies (BEs) compared to previously reported peak positions for isolated graphene. This BE upshift is indicative of coupling between the Cu catalyst and the growing graphene. The higher BE is retained after hydrocarbon exposure and cooling, but lost during air/oxygen exposure due to oxygen intercalation which decouples the Cu

Received: June 27, 2013
Revised: September 10, 2013
Published: September 16, 2013

 © 2013 American Chemical Society

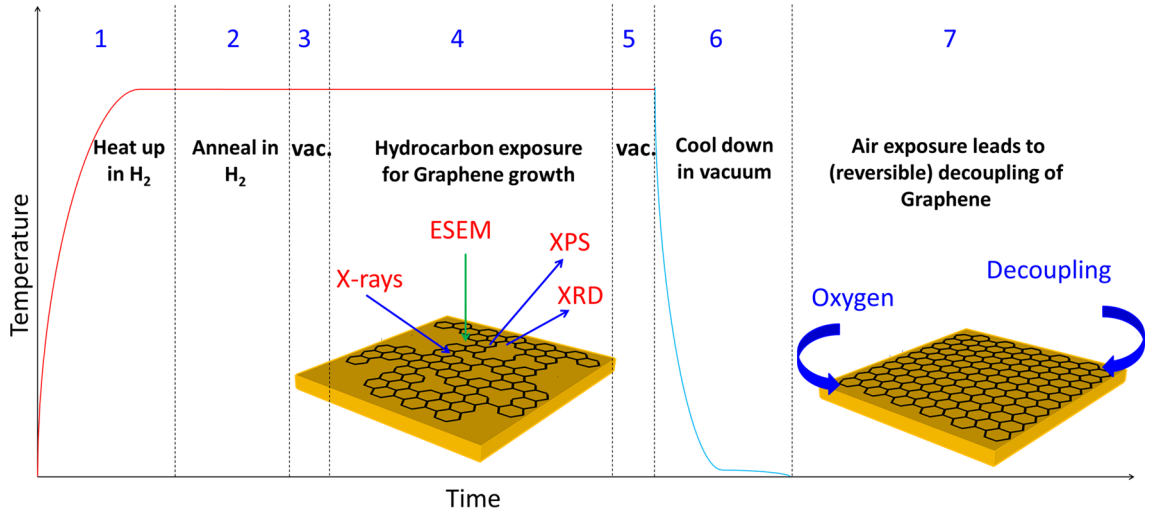

Figure 1. Schematic process diagram illustrating the salient stages of graphene CVD on polycrystalline Cu studied using in situ XPS, XRD, and ESEM.

and MLG. We show that the Cu-MLG decoupling can be reversed and coupling can be restored by vacuum annealing. We observe that the presence of residual oxygen in the CVD atmosphere can also lead to a change in the MLG−Cu interaction. Our in situ measurements also indicate a minor carbon uptake into the Cu bulk which under certain conditions can manifest itself as carbon precipitation upon cooling and hence deserves consideration as part of a holistic understanding of graphene CVD.

Results. Using complementary in situ XPS, ESEM, and XRD, we capture the evolution of the MLG-Cu surface chemistry and morphology, the Cu bulk crystallography, and the MLG-Cu interactions at each stage of graphene CVD and subsequent air exposure. Figure 1 summarizes the salient steps (1−7). For the majority of the MLG growth experiments in this study undiluted C_6H_6 vapor (at $P_{C_6H_6} \sim 1 - 5 \times 10^{-3}$ mbar, after ∼0.2 mbar H_2 pretreatment) and a growth temperature of ∼900 °C were used (unless specified otherwise). We have previously established that these CVD conditions result in MLG of a quality comparable to state-of-the-art graphene,[3] and we note that all in situ grown samples from our standard CVD conditions show ex situ Raman signatures corresponding to MLG of comparable quality (see below). For experimental details see the Methods section below.

Graphene Growth. Figure 2a shows the evolution of the C1s XP spectra during CVD using C_6H_6 (steps 3−6), complemented by laterally resolved morphological information from a sequence of in situ ESEM images (Figure 2c). Following pretreatment in H_2 and vacuum (steps 1−3) we obtain a flat line in the C1s scan implying a carbon free Cu surface given the experimental sensitivity. The catalyst surface exhibits contrast differences in the ESEM image arising from different Cu grains. Upon C_6H_6 exposure, after ∼140 s, we observe the rise of a small intensity in the C1s XP spectra centered at 284.75 eV (labeled C_1). Two additional components appear at binding energies of 285.2 (labeled C_2) and 284.4 eV (labeled C_3) after ∼470 s. C_1, C_2, and C_3 reflect the presence of several distinct carbon binding arrangements on the Cu surface during growth. All peaks increase with ongoing C_6H_6 exposure, keeping approximately the same intensity ratio to each other, which remains largely unchanged upon C_6H_6 removal at temperature (step 5) and during subsequent cooling in vacuum (step 6). The ESEM images reveal the formation of graphene nuclei upon C_6H_6 exposure, which continue to grow in lateral size with increasing exposure time to form multilobed graphene islands,[5,26] before merging to form a continuous film. Based on the postgrowth Raman characterization of the in situ samples (see Figure 2b), we confirm MLG growth [2D (2688 cm^{-1}), G (1589 cm^{-1}), and D (1355 cm^{-1}) peaks, where the 2D peak can be fitted with a single Lorentzian curve and $I_{2D}/I_G > 2$] of reasonably high quality ($I_D/I_G \sim 0.1$). The combination of our XPS, ESEM, and Raman data confirms isothermal MLG growth during hydrocarbon CVD.

We assign C_1, the dominant component in the in situ C1s signal, as the XPS fingerprint of as-grown graphene on polycrystalline Cu (i.e., before removal to ambient air). This C_1 component has a BE that is distinctly different from the commonly reported ex situ measured C1s peak position for graphene grown on Cu at 284.4 eV[27] (which matches our C_3 component). Interestingly, when remeasuring the in situ grown samples after ambient air exposure at room temperature for ∼45 min (step 7), we find a shift in the dominating C1s peak component toward C_3 at 284.4 eV, along with an increase in the oxygen O1s signal (see Figure 3c). Previous reports have suggested that Cu in direct contact with MLG leads to n-type doping of the MLG due to charge transfer,[28−32] which presents an interpretation of the BE shift.[33−36] We note however that our observed shifted BE, that is, the C_1 at 284.75 eV, could also be rationalized by exchange interactions between the Cu valence electronic structure and the C1s core hole, that is, spectroscopically a final state effect rather than a ground state effect. In any case, the recovery of the free-standing graphene signal post air exposure to C_3 at 284.4 eV and concurrent appearance of an O1s signal (see Figure 3c) is clearly indicative of oxygen intercalation (see below). Therefore we assign C_1 (284.75 eV) to MLG growing in a *coupled* state and C_3 (284.4 eV) to MLG in a *decoupled* state (i.e., oxygen intercalated between MLG and Cu). We emphasize that the terms "coupled" and "decoupled" are here used as relative descriptions for graphene in direct contact with Cu and graphene with intercalated oxygen on Cu, respectively. These terms do not imply that the interaction between MLG/Cu ("coupled") is stronger than the previously theoretically estimated weak bonding.[6,30] We note that the binding energy

dx.doi.org/10.1021/nl4023572 | *Nano Lett.* 2013, 13, 4769−4778

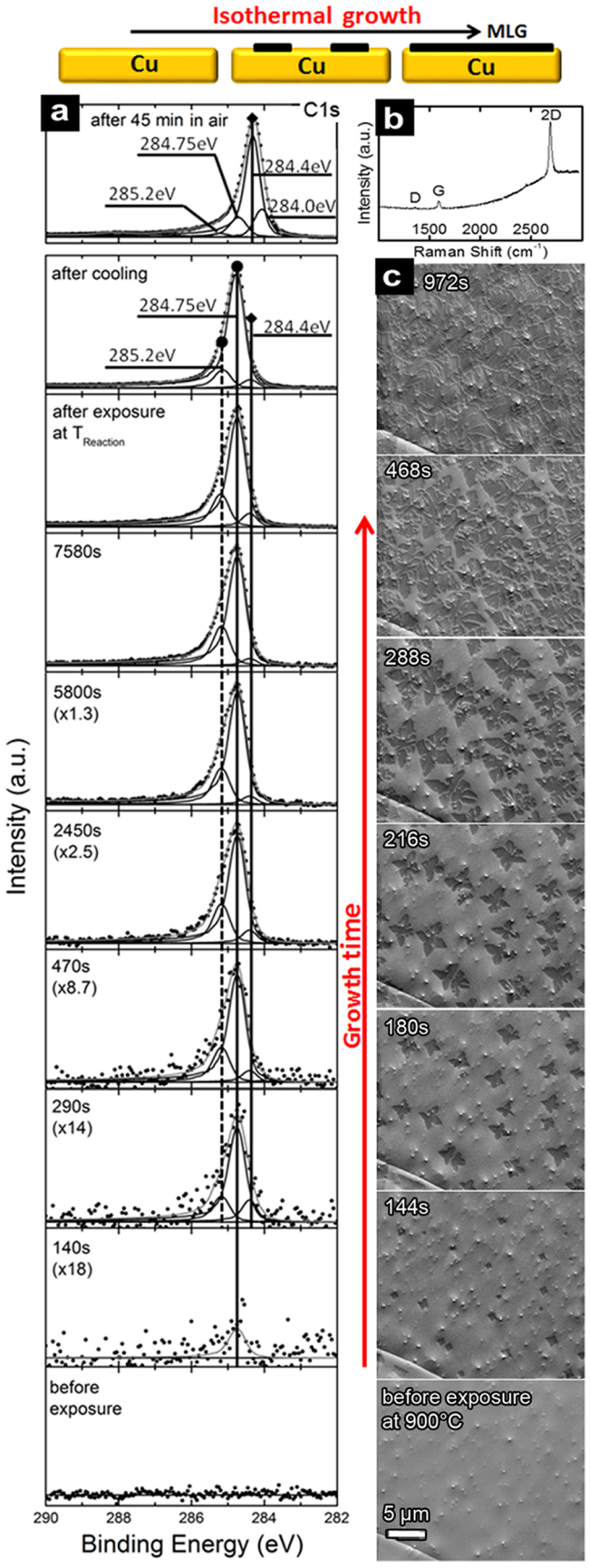

Figure 2. Isothermal graphene growth on Cu: (a) in situ time-resolved XPS C1s core level scans at 900 °C before (step 3), during (step 4), and after hydrocarbon (C_6H_6) exposure (step 5), after cooling (step 6), and after air exposure (step 7). The numbers in brackets indicate multipliers for intensities of separate scans. (b) Raman spectrum obtained from the in situ grown graphene in part a, typical for all in situ grown MLG. (c) Corresponding time-resolved in situ ESEM image sequence for graphene growth on Cu before (step 3) and during (step 4) hydrocarbon (C_6H_6) exposure at 900 °C. Time stamps in a and c refer to time elapsed after hydrocarbon introduction.

offset between C_1 and C_2 is +0.45 eV, which is consistent with the commonly reported offset between graphene and deleterious carbon (sp^3-hybridized carbon),[37,38] and hence assign C_2 to defects in the growing graphene. Based on the Raman data in Figure 2b ($I_D/I_G \sim 0.1$), the C_2 signal level presented here corresponds to MLG with a reasonably low defect density.

From our XPS assignments, we find that graphene predominantly grows isothermally during CVD coupled to Cu (C_1) with a small amount of defects in the graphene (C_2) and with a small fraction of the layer decoupled (C_3). When graphene on Cu is then air-exposed at room temperature after CVD, the MLG layer is decoupled via oxygen intercalation (shift of the majority of the C1s signal to C_3 position). We will further corroborate this assignment and present details of the oxygen intercalation below.

Compared to the C1s evolution on the relatively higher carbon solubility catalyst Ni,[37,38] we observe no XPS signatures of other carbon species (e.g., metastable surface carbides or carbon dissolved in the catalyst) before the coupled graphene fingerprint C_1 starts to rise. The lack of these features on Cu indicates a growth mechanism in which carbon incorporation into the catalyst subsurface is considerably reduced compared to Ni. This is in broad agreement with the model previously suggested by indirect ex situ experiments[4] and in situ LEEM studies during nonhydrocarbon based graphene growth[26] where negligible carbon was measured before graphene nucleation was observed. We note that our XPS peak evolution observed during CVD (i.e., coupled graphene fingerprint C_1 appearing without significant other contributions) is not limited to C_6H_6 growth but is also detected for CH_4-and C_2H_4-based CVD (not shown here), implying that this evolution type is generic for catalytic CVD of graphene using hydrocarbons on Cu catalysts. Similarly, we measure the shift of the C1s majority component to the decoupled C_3 position upon air exposure not only for C_6H_6-grown MLG but indeed for any CH_4- and C_2H_4-grown MLG films[3] on Cu investigated in this study, confirming that the decoupling of graphene upon room temperature air exposure is also a generic phenomenon on polycrystalline Cu catalysts.

In addition to the carbon fingerprint, in situ XPS allows us to simultaneously examine the chemical state of the Cu catalyst surface. Figure 3a, b and c shows spectra of the Cu LMM Auger region, Cu $2p_{3/2}$, and O1s spectra, respectively, for as-loaded Cu foils (before step 1), after H_2 anneal (step 3), during C_6H_6 exposure (step 4), after cooling in vacuum (step 6), and after post-CVD air exposure (step 7). The as-loaded Cu foil is oxidized from storage in ambient air, as revealed by the typical Cu_2O Auger LMM fingerprint spectrum (Figure 3a).[39,40] The corresponding O1s (Figure 3c) and C1s (not shown) spectra exhibit OH-groups as well as adventitious carbon and H_2O adsorption.[41−43] Annealing in H_2 removes carbon adsorbents[44,45] as seen by the initial flat line in Figure 2a and reduces the Cu to a metallic surface (development of typical LMM

dx.doi.org/10.1021/nl4023572 | Nano Lett. 2013, 13, 4769−4778

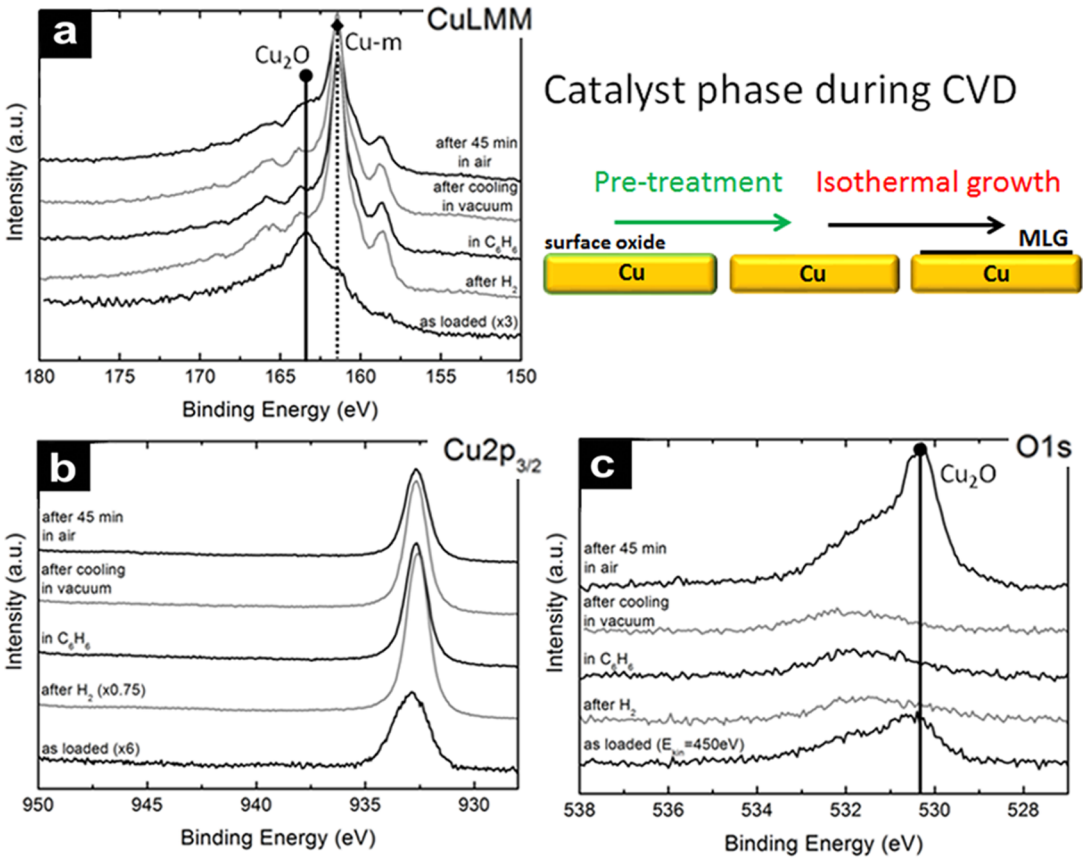

Figure 3. Surface chemistry of the Cu catalyst as loaded (before step 1), after H_2 anneal (step 2), during hydrocarbon exposure (step 4), after cooling in vacuum (step 6), and after ambient air exposure (step 7) using (a) in situ XPS Cu LMM Auger, (b) Cu $2p_{3/2}$, and (c) O1s spectra [note that the as-loaded O1s scan was measured at a higher kinetic energy (450 eV) to penetrate the adventitious carbon from ambient air storage]. The numbers in brackets indicate multipliers for intensities of separate scans. Comparing a and b, we note that the Cu LMM Auger is more sensitive to changes in the oxidation state of Cu than the Cu $2p_{3/2}$ spectra.

spectrum of reduced Cu in Figure 3a) leaving only minor traces of OH bonds (Figure 3c).[39,40] Upon hydrocarbon exposure and graphene growth no changes develop in the Cu LMM, Cu $2p_{3/2}$, and O1s XP spectra, indicating that metallic Cu is the active catalyst state. Notably, compared to Ni,[37,38] no significant signatures of dissolved carbon are observed during growth (corroborating the C1s assignments).

To complement the surface-sensitive XPS (information depth 0.7−1.2 nm), we use bulk-structure-sensitive in situ XRD during salient stages of CVD (Supporting Figure S1a, information depth ∼5 μm). As-loaded Cu shows reflections corresponding to metallic face-centered-cubic (fcc) Cu. Upon heating in H_2 (step 2) we observe a decrease in the peak width in the fcc Cu, consistent with crystallization and grain growth. The peak widths approach the instrumental resolution of the XRD setup, implying the formation of large grains. This is consistent with previous literature[3,5,46] and observations during heating in the ESEM (not shown here). Upon exposure to C_6H_6 during graphene CVD we find that metallic fcc Cu remains as the only detectable catalyst phase, further confirming that metallic Cu is the active catalyst state both on the catalyst surface and in the bulk.

Cycling between Air Exposure and Vacuum Annealing. Having established isothermal graphene growth on Cu and the metallic catalyst state we now return to elucidate the details of the decoupling of the MLG from Cu via oxygen intercalation. For the XP spectra in Figure 4a, we measure an ex situ C_6H_6 grown full coverage MLG film on Cu[3] after ambient air exposure for ∼4 weeks. As loaded the air-exposed MLG on Cu exhibits a well-defined decoupled C_3 component at ∼284.4 eV, accompanied by three minor peaks at 285.2, 284.75, and 284.0 eV. This fingerprint is consistent with the spectrum after air exposure in Figure 2a. We note that the latter peaks are partly overlapping with the BEs of C_1 and C_3 but are also the known BEs of adsorbed adventitious carbon from ambient air exposure.[47−49] The corresponding O1s (Figure 4b), CuLMM, and valence band spectra (Supporting Figure S2a and b, respectively) of the as-loaded MLG sample show a mixture of Cu_2O (solid line in Figure 4b, at ∼530.2 eV[42,50,51]), OH groups and H_2O.[41,42,52]

Heating stepwise in vacuum (∼10^{-7} mbar), first to 150 °C (not shown) there is no change in the C1s and O1s, and Cu remains oxidized. Upon reaching 500 °C the C1s changes: The components at 285.2, 284.75, and 284.0 eV disappear, and the remaining majority component is C_3 at 284.4 eV corresponding to decoupled graphene. Therefore, *for air-exposed, as-loaded samples* the components at 285.2, 284.75, and 284.0 eV are assigned to adventitious carbon. The O1s spectrum also changes to exhibit a shift of the main intensity to ∼529.7 eV (dashed line), indicating the onset of Cu-oxide reduction. With further heating to 700 °C the C1s spectrum changes dramatically: The C1s main component shifts to 284.74 eV, that is, recovers the C_1 position corresponding to coupled graphene, and a small shoulder at C_2 (285.2 eV) emerges.

dx.doi.org/10.1021/nl4023572 | *Nano Lett.* 2013, 13, 4769−4778

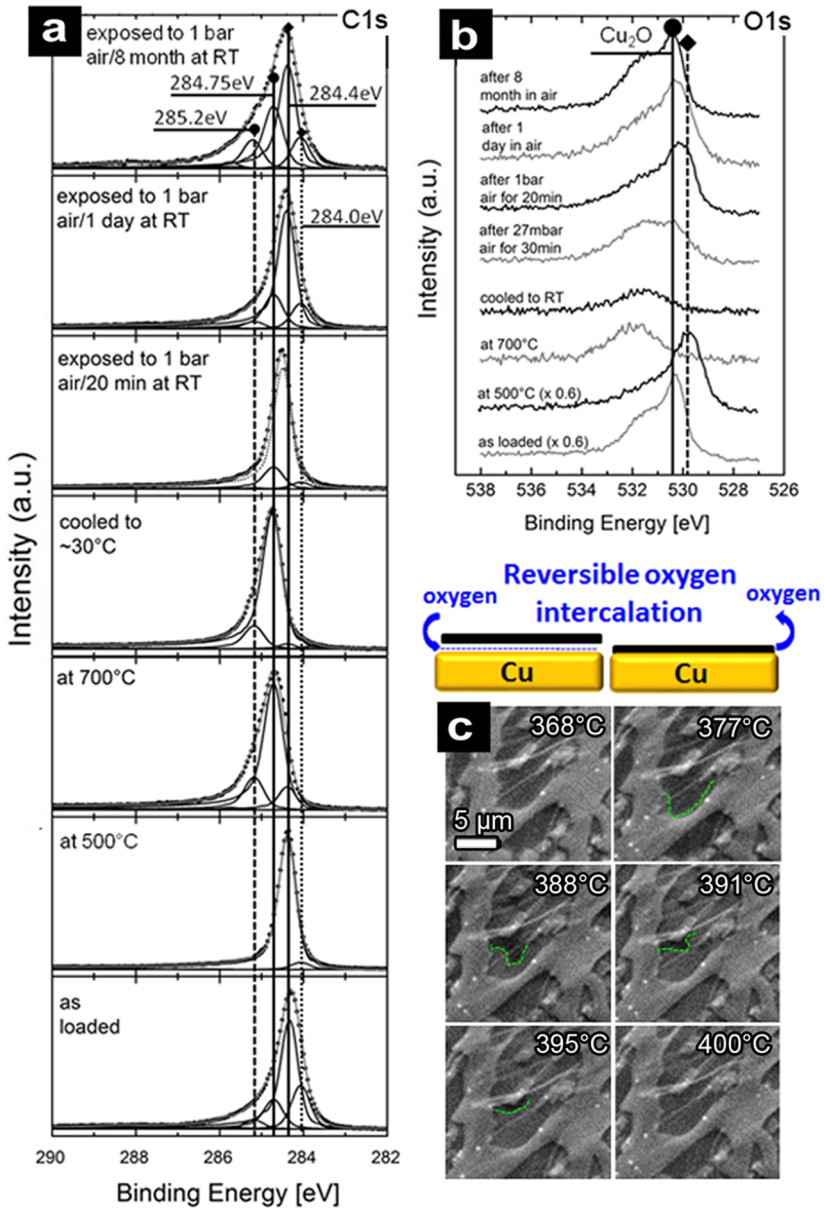

Figure 4. Coupling and decoupling of graphene on Cu via oxygen intercalation as measured using in situ XPS for the (a) C1s and (b) O1s region (where the circle and diamond represents the BEs of Cu_2O and CuO, respectively). (c) ESEM image sequence of ex situ grown, air transferred graphene nuclei on Cu during annealing in vacuum. Within the nuclei, regions of dark contrast are attributed to decoupled graphene and areas of light contrast to coupled graphene. Note that the green dashed line is a guide to the eye.

Concurrently, the C_3 peak (284.4 eV) is drastically reduced. The XP spectrum now resembles the in situ acquired spectrum *during* graphene growth in Figure 2a. The corresponding O1s at ~700 °C shows the reduction of Cu, where only some residual minor traces of OH bonds remain at ~531−532 eV,[39,40] resembling the O1s spectra acquired during growth (Figure 3c). This shows that by vacuum annealing the decoupling of the graphene by the oxygen interlayer can be reversed and that the graphene can be recoupled to Cu.

When cooling the annealed sample to room temperature in vacuum the C1s spectrum does not change and remains at the coupled C_1 position (as post-CVD in Figure 2a). Only, upon subsequent exposure to ambient air at room temperature the composition of the C1s spectra changes again with the major peak component shifting back from C_1 toward C_3. After 20 min of air exposure an intermediate state between C_1 and C_3 is reached with the highest intensity located at ~284.45 eV. After one day in air the original state of the as-loaded sample is approached with the highest intensity at the C_3 position, and after eight months in air we measure the same C1s peak positions with a majority C_3 as in the initially loaded sample (with an increasing contamination contribution from adventitious carbon due to the longer storage in ambient air). Air exposure correspondingly leads to a reoxidation of the Cu (Figure 4b and Supporting Figure S2). While after storage in air for 1 day a less intense Cu_2O contribution is observed than for the as loaded sample, after storage in ambient air for 8 months the initial oxidation state of the Cu is reached.

To visualize the morphological dynamics of this recoupling process we perform the same air exposure/vacuum annealing cycling of ex situ grown MLG islands using ESEM. Figure 4c shows that for islands the recoupling temperature is reduced by

dx.doi.org/10.1021/nl4023572 | *Nano Lett.* 2013, 13, 4769−4778

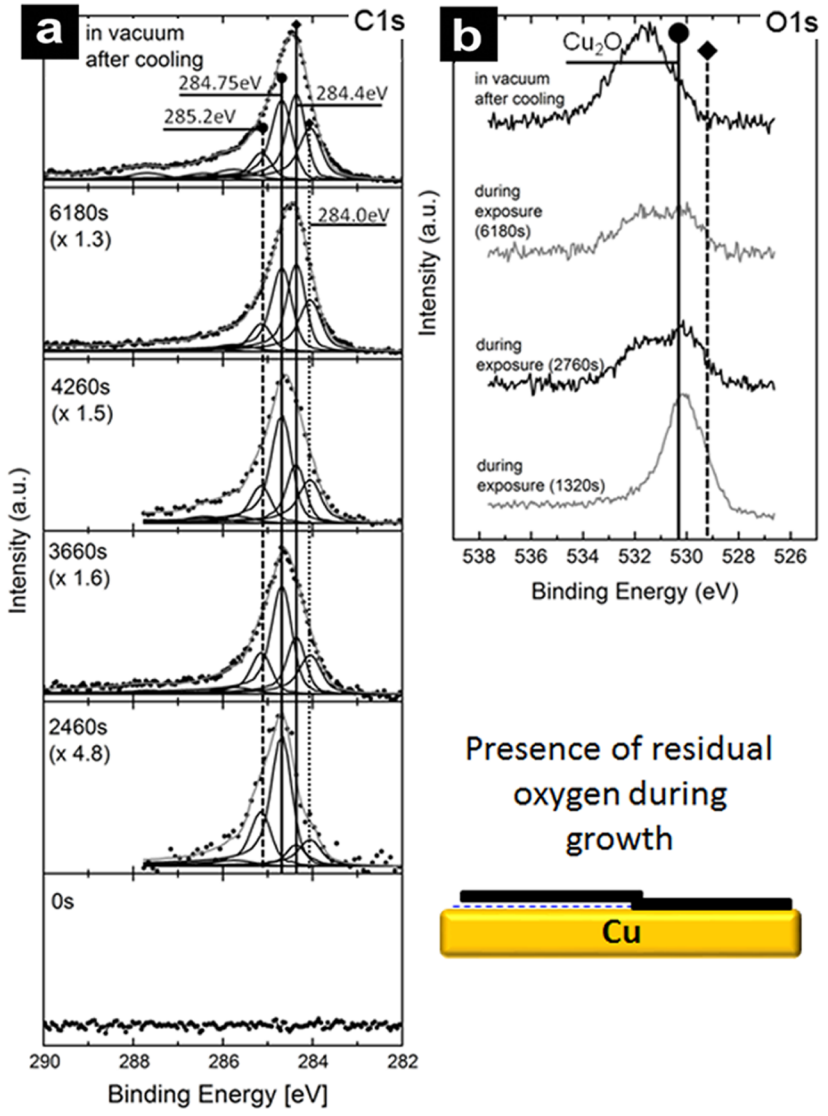

Figure 5. Graphene growth on Cu with residual air in the CVD atmosphere. (a) Time-resolved C1s scan during C_6H_6 exposure. Time stamps refer to time elapsed after hydrocarbon introduction. The numbers in brackets indicate multipliers for intensities of separate scans. (b) O1s core level XP scans at 900 °C during (step 4) C_6H_6 exposure and after cooling in vacuum (step 6) where the circle and diamond represents the BEs of Cu_2O and CuO, respectively.

~200 °C compared to the full coverage film (also confirmed by in situ XPS on MLG islands, not shown) and that recoupling starts at an island's edges and proceeds inward, as seen by the indicated change in SEM contrast.

By comparing the C1s intensities we determine a maximum loss of carbon <10% from the MLG layer during vacuum annealing. We emphasize that we do not observe any loss of flake size in ESEM during annealing (Figure 4c). This suggests that diffusion/direct-desorption may be the dominating processes for oxygen removal from underneath the MLG while carbon-mediated oxygen loss plays a minor role for the first cycle.[53,54] Minor reactions with the MLG are however also observed in our data since with increasing cycling temperature we observe a small increase in the C_2 component at 285.2 eV (Figure 4a at 700 °C). Corroborating our previous assignment of C_2 to defects in coupled graphene, this small intensity increase suggests that a small level of defects is introduced into the graphene by reannealing in vacuum. Raman measurements on cycled graphene films show a minor increase in D-band intensity, implying that for a single reanneal cycle structural damage to the graphene remains limited.

Our findings on reversible oxygen intercalation between MLG and polycrystalline Cu are consistent with the suggestion of oxygen intercalation for Cu single crystals[28] and with previous literature for MLG on Ir[53,55] and Ru.[54,56] We suggest the intrinsically polycrystalline nature of CVD graphene can offer pathways for gas species diffusion.[3,57] Our findings also explain the reappearance of Cu surface states in STM after vacuum annealing of air transferred graphene on Cu.[58] While our current measurements do not reveal the full details of the state of the intercalated oxygen species such as adsorption geometries/sites and possible surface reconstructions, we note that previously reported room temperature Cu-bulk oxidation under polycrystalline MLG layers[15−19] is a different process to the oxygen intercalation reported here. Bulk oxidation has a very different time scale (days to weeks) compared to the oxygen-intercalation-related decoupling of MLG which happens much faster (minutes to hours). Clearly however, oxygen

dx.doi.org/10.1021/nl4023572 | Nano Lett. 2013, 13, 4769−4778

intercalation is the first step of Cu-bulk oxidation.[59] (see Supporting Figure S3.)

In the previous sections we established that under standard CVD conditions MLG grows in a coupled mode on fully reduced Cu and that air exposure quickly leads to decoupling of graphene. As a further step we now investigate changes in our observations for conditions that differ from standard CVD. In particular, we look at the effect of residual gases in the CVD atmosphere and on the effect of extended hydrocarbon exposures below the MLG nucleation threshold on the Cu bulk.

Effect of Residual Air Contamination in CVD Atmosphere. By employing a less stringent freeze−pump−thaw cleaning of the liquid C_6H_6 reservoir, an air bubble precedes graphene nucleation when the C_6H_6 vapor is introduced. We first pretreat Cu in H_2 (step 1−3) leading to a reduced catalyst (similar as in Figures 2 and 3). Then, as shown in Figure 5 we introduce the air contaminated C_6H_6 vapor at the growth temperature into the chamber and observe via mass spectrometry an air bubble to flow through the CVD chamber (see Supporting Figure S4a for mass spectrometer data). This leads to partial reoxidation of the Cu (O1s, see Figure 5b) and strongly increases the incubation time of graphene growth (to ∼1000 s). During this incubation time, partial re-reduction of the Cu catalyst (Figure 5b) is observed in the O1s XP spectra. Then, at a point where the oxygen level is still higher than in our standard C_6H_6 exposure (Figure 3c), graphene nucleates as seen by the rise in the C1s (Figure 5a). The key observation here is that the graphene is initially coupled (C_1 appearing first) but then during isothermal growth the C1s intensity shifts to the C_3 position of decoupled graphene, resulting in roughly half of the intensity at C_1 and C_3, respectively. This is unlike our standard exposure where C_3 only becomes a significant component upon air exposure after growth. Alongside the majority C_1 and C_3 components, we also observe 285.2 eV (C_2) and 284.0 eV contributions during growth, which we assign to defects in the graphene (as adsorption of adventitious carbon can be excluded during the in situ scans). The defect contributions in the graphene signal are higher for this "air bubble exposure" compared to the standard growth from Figure 2a (confirmed by ex situ Raman spectroscopy, not shown).

The growth of graphene on a partially oxidized Cu surface corresponds well to previous ex situ reports of MLG growth on (partial) Cu surface oxides.[3,60,61] The integral nature of our XPS measurements does not allow distinguishing whether at this temperature the graphene nucleates first coupled and subsequently gets decoupled or whether graphene already nucleates in the decoupled state. Nevertheless, while we find the presence of oxygen to lead to increased defect levels in the growing graphene (which is expected), the unexpected shift in the C1s majority component when residual oxygen is present highlights that residual gases in the CVD atmosphere can induce a change in the graphene−Cu interaction.

Involvement of Cu Bulk. Finally, we address the question of bulk involvement of Cu catalysts during graphene growth. Compared to Ni,[37,38] our XPS and XRD data do not show significant signs of carbon dissolution in Cu during our standard CVD processing. This is in agreement with reports for Cu catalysts where precipitation of dissolved carbon upon cooling was generally perceived to be negligible.[4] The reported values of carbon solubility in Cu (at ∼1000 °C between 0.00070 atom %[62] and 0.028 atom %[63]) however suggest that the amount of carbon dissolved in a 25 μm Cu foil (as used in our experiments) can correspond to between 0.4 and 15.5 layers of graphene (atomic density of carbon $\sim 3.8 \times 10^{19}$ atoms m^{-2}). This is a surprisingly large number of layers that potentially could precipitate due to a reduction of the solubility upon cooling, particularly since previously reports have been divided on whether small amounts of precipitation were observed[64] or not.[4,5,7] Also theoretical calculations recently addressed the possible role of subsurface carbon species in the Cu catalyst during MLG growth.[65,66] In this context, we carried out a set of experiments whereby the Cu foil is exposed for extended times to low C_6H_6 pressures ($P_{C_6H_6} < 1 \times 10^{-4}$ mbar). For such exposures in situ XPS shows no peaks emerging in the C1s region (for the 40 min probed); that is, no graphene is nucleated isothermally (Supporting Figure S5a). However, upon subsequent cooling in vacuum we observe the appearance of a small broad C1s signal which increases with falling temperature, indicative of carbon precipitation upon cooling. Similar exposures in the ESEM (Supporting Figure S5b,c) show carbon precipitation upon slow cooling in the form of a pattern of speckles (<0.1 μm^2). Notably, the features formed by precipitation are not limited to Cu grain boundaries[64] but are located across the Cu grains. The precipitated carbon is hardly detectable with Raman spectroscopy on Cu (not shown). Hence our data indicate that under certain conditions minor carbon precipitation upon cooling, here in the form of deleterious defective carbon, can be observed for Cu foils.

Discussion. Our in situ data offers unprecedented insights into the growth and interaction mechanisms of MLG on Cu and has a number of important implications for future optimization of Cu-catalyzed graphene CVD as well as for subsequent processing and device integration.

Post-CVD, MLG is quickly decoupled over a time scale of minutes to hours from the Cu by oxygen intercalation in ambient air even at room temperature. This decoupling is reversible by simple vacuum annealing. The ease of oxygen mediated decoupling implies that experimental determination of the Cu-graphene interaction strength[6,11,20−22] needs to carefully account for any unintentional oxygen exposure, not to underestimate the already weak[30,31] graphene−Cu interaction. The observed oxygen intercalation also has important ramifications regarding the possible need for cluster-tool processing when using MLG directly on the Cu catalyst, as in, for example, contacts.[23,24] Also the currently debated wetting transparency of graphene might be affected by the observed coupling/decoupling mechanisms.[20−22] We note that to characterize Cu-oxidation under MLG in sufficient detail by XPS the CuLMM signal is more sensitive than the Cu $2p_{3/2}$ signal and less ambiguous than the O1s signal.[15,17,21] Cu $2p_{3/2}$ core-level measurements alone are insufficient to detect our observed intercalation (which can be seen by comparing Figure 3a−c). With regard to the debated use of graphene as a protective layer against corrosion,[15−19] our data shows that even for high-quality continuous CVD MLG films gaseous species do reach the MLG-Cu interface over a relatively short time scale. This implies that corrosion of Cu under MLG in ambient air is a multistep phenomenon comprised of the very fast initial intercalation (as shown in this work), followed by short-term dry-corrosion-protection[15,16] and then long-term degradation via wet oxidation.[16,19] Our data further indicates that even trace amounts of oxygen present in a CVD reactor can alter the MLG−Cu interactions, which might eventually affect the graphene growth results. This might be an important factor to rationalize some of the many different reported results

dx.doi.org/10.1021/nl4023572 | Nano Lett. 2013, 13, 4769−4778

on process-dependent relationships between the Cu surface and MLG domain shape and orientation.[8−13] Hence residual contamination levels during CVD may have to be carefully addressed for further optimization of controlled graphene growth.[61]

Our data highlight that during standard CVD graphene dominantly grows isothermally in a coupled mode on reduced Cu. We note that in contrast to catalysts that have a higher carbon solubility and/or interact more strongly with carbon (such as Ni[37,38]), we do not observe XPS signatures corresponding to a carbide surface reconstruction or to a substantial carbon uptake into the catalyst bulk or subsurface under our standard exposure and cooling conditions. This appears to fit with the proposed surface model of graphene growth on Cu,[1] which is typically contrasted to a model of growth by precipitation upon cooling for higher carbon solubility catalysts like Ni.[4] We have previously however already highlighted that for Ni this perceived binary picture is incomplete, as for instance at low temperatures an isothermal growth regime is dominant for Ni.[37,38] The dominating growth mode between isothermal and precipitation growth from Ni was in fact found to be highly dependent on process conditions, such as temperature, heating profiles, catalyst thickness, and other kinetic factors.[67] In this context, we proposed a kinetic growth model considering the flux balance between carbon reaching and leaving the catalyst surface.[67] Our data here including the observation of precipitated carbon from Cu, be it minor, implies that such a kinetic model is also applicable to Cu. This also suggests that unintentional carbon uptake from, for example, deleterious carbon deposits present in most CVD systems[68] or from the processing history of commercial Cu catalyst foils may alter the growth characteristics of graphene on Cu. Likewise, in an earlier report on bilayer graphene growth on Cu[69] the main process modification employed to obtain bilayer (and not monolayer) graphene had been a slower cooling rate after CVD, possibly consistent with precipitation-mediated carbon nucleation. In any case, the combination of our previous reports on Ni[37,38,67] and our findings here imply that the fundamental routes to graphene growth on lower carbon solubility catalysts (like Cu) are not as different from those of higher carbon solubility catalysts (like Ni) as has often been stated in literature.[4,6]

In summary, we used a range of complementary in situ techniques to reveal the highly dynamic nature of MLG-Cu interactions throughout the entirety of the graphene CVD process on polycrystalline Cu catalysts. In particular, our detailed in situ observations of the surface chemistry evolution during isothermal MLG growth and of the ease of oxygen intercalation between MLG and Cu under ambient conditions provide important implications for future optimization of graphene manufacturing and device integration.

Methods. Graphene CVD using C_6H_6, CH_4, and C_2H_4 as hydrocarbon precursors was performed in customized in situ-compatible cold-wall CVD reactors on commercially available cold rolled polycrystalline Cu foils (Alfa Aesar, 25 μm thick 99.999% purity), based on earlier reported recipes.[3] The majority of this study uses (unless specified otherwise) exposures in undiluted C_6H_6 vapor (fed via a leak valve from a liquid C_6H_6 reservoir, cleaned from residual air by repeated freeze−pump−thaw cycles) at $P_{C_6H_6} \sim 1 - 5 \times 10^{-3}$ mbar and ~900 °C, while for cross-checks with CH_4/H_2 and C_2H_4 total exposure pressures of 0.2 mbar were used. The CVD process typically included a H_2 pretreatment step (~0.2 mbar), followed by a quick pump-down to base pressure before introducing the carbon precursor as summarized in Figure 1.

In situ XPS measurements during C_6H_6, CH_4, and C_2H_4 CVD were performed at the BESSY II synchrotron at the ISISS end station of the FHI-MPG.[70] A differentially pumped XPS system allows CVD at pressures up to 1 mbar while measuring in situ XPS (base pressure < 10^{-7} mbar). Cu catalyst foils were clamped with SiC clips onto SiO_2 (300 nm)/Si wafers and heated via an IR laser focused onto the backside of the wafer. Temperature readings were taken via a precalibration with a thermocouple and cross-checked with pyrometer measurements during CVD (±30 °C of reported temperature). The reaction atmosphere composition was continuously monitored using a mass spectrometer (Prisma). Time-resolved XPS core level spectra of the C1s, Cu 2p, O1s regions, Cu LMM Auger region, and the valence band region were acquired at salient stages of CVD at two sets of electron kinetic energies at 150 and 450 eV corresponding to information depths of ~0.7 nm and ~1.2 nm, respectively.[71] We note that all peak positions reported in this study were referenced to the simultaneously acquired Fermi edge. Spectral resolution was ~0.3 eV. Background correction was performed by using a Shirley background.[72] C1s spectra were fitted following the Levenberg−Marquardt algorithm to minimize the χ^2. Peak shapes were modeled by using asymmetric Doniach−Sunjic functions convoluted with Gaussian profiles[73] featuring an asymmetry parameter of α = 0.09, which result in the best fit for all components. The accuracy of the fitted peak positions is ~0.05 eV.

In situ ESEM experiments using C_6H_6 were performed at the Fritz-Haber-Institut of the Max-Planck-Society in a commercial ESEM (FEI Quantum 200, base pressure ~1×10^{-6} mbar) with a heating stage and gas supply unit (Bronkhorst). Temperatures were measured with a thermocouple spot-welded to one far end of a thin Cu foil strip and have an estimated uncertainty of ±30 °C. Samples were imaged using a standard Everhart−Thornley detector and an acceleration voltage of 5.0 kV during H_2 pretreatment and C_6H_6 growth, while the CVD atmosphere was monitored by a mass spectrometer (Pfeiffer OmniStar).

In situ XRD (Theta−2Theta geometry) during pretreatment and C_6H_6 CVD was performed at the BM20 beamline (Rossendorf beamline) of the European Synchrotron Radiation Facility (ESRF) in a cold-wall reactor chamber mounted on a high-precision six-circle goniometer (base pressure ~10^{-6} mbar). The stainless-steel reactor chamber has Kapton windows fitted to allow transmission of X-rays in different scattering geometries. A Si (111) double crystal monochromator was used to select the X-ray energy (monochromatic X-ray beam of 11.5 keV with a corresponding wavelength of 1.078 Å). The diffracted X-rays were measured using a horizontally aligned Soller slit system and a one-dimensional line detector (K-Tek). Since the high degree of texture in cold rolled Cu foils prevents reliable measurement in powder-diffraction geometry, Cu powder (Alfa Aesar, <5 μm, 99.9% purity) pressed into a thick granular film onto a sapphire wafer was used as a catalyst model system for the in situ XRD experiments. A boron nitride coated graphite resistive heating element (Boralectric) was used to heat the sample clamped down with alumina spacers, and the temperature was measured with a thermocouple in contact with the sapphire substrate (uncertainty ±30 °C of reported

dx.doi.org/10.1021/nl4023572 | Nano Lett. 2013, 13, 4769−4778

temperature). Note that monolayer graphene is not detectable in the used XRD setup.

Graphene growth from all in situ experiments was confirmed by ex situ characterization using scanning electron microscopy (SEM, Carl Zeiss SIGMA VP, 1−2 kV) and Raman spectroscopy (custom built Raman set up using a 488 nm Ar laser with 1.1 mW on the sample).

We cross-checked XPS signatures and performed additional in situ heating experiments using ex situ grown MLG and few-layer graphene including samples with full coverage and only island coverage, all grown in a cold-wall CVD system using C_6H_6 or CH_4 as the carbon precursors.[3]

■ ASSOCIATED CONTENT

Supporting Information

XRD and Raman data for the in situ XRD experiment; additional in situ XPS data for the cycling experiments; optical images for Cu bulk oxidation experiments; mass spectrometry data and additional in situ XPS data for the "air bubble exposure" experiment; in situ XPS and ESEM data and detailed description for the carbon precipitation experiments. This material is available free of charge via the Internet at http://pubs.acs.org.

■ AUTHOR INFORMATION

Corresponding Author

*E-mail: sh315@cam.ac.uk.

Notes

The authors declare no competing financial interest.

■ ACKNOWLEDGMENTS

S.H. acknowledges funding from ERC grant InsituNANO (no. 279342), EPSRC grant GRAPHTED (project reference EP/K016636/1), and grant EP/H047565/1. This research was partially supported by the EU FP7 Work Programme under grant GRAFOL (project reference 285275). We acknowledge the Helmholtz-Zentrum-Berlin Electron storage ring BESSY II for provision of synchrotron radiation at the ISISS beamline, and we thank the BESSY staff for continuous support of our experiments. We acknowledge the European Synchrotron Radiation Facility (ESRF) for provision of synchrotron radiation, and we thank the staff for assistance in using beamline BM20/ROBL. P.R.K. acknowledges funding from the Cambridge Commonwealth Trust, B.C.B. acknowledges a Research Fellowship at Hughes Hall, Cambridge, and R.S.W. acknowledges funding from EPSRC (Doctoral training award) and the Nano Science & Technology Doctoral Training Centre Cambridge (NanoDTC).

■ REFERENCES

(1) Li, X.; Cai, W.; An, J.; Kim, S.; Nah, J.; Yang, D.; Piner, R.; Velamakanni, A.; Jung, I.; Tutuc, E.; Banerjee, S. K.; Colombo, L.; Ruoff, R. S. *Science* **2009**, *324*, 1312−1314.

(2) Bae, S.; Kim, H.; Lee, Y.; Xu, X.; Park, J.-S.; Zheng, Y.; Balakrishnan, J.; Lei, T.; Ri Kim, H.; Song, Y. I.; Kim, Y.-J.; Kim, K. S.; Ozyilmaz, B.; Ahn, J.-H.; Hong, B. H.; Iijima, S. *Nat. Nanotechnol.* **2010**, *5*, 574−578.

(3) Kidambi, P. R.; Ducati, C.; Dlubak, B.; Gardiner, D.; Weatherup, R. S.; Martin, M.-B.; Seneor, P.; Coles, H.; Hofmann, S. *J. Phys. Chem. C* **2012**, *116*, 22492−22501.

(4) Li, X.; Cai, W.; Colombo, L.; Ruoff, R. S. *Nano Lett.* **2009**, *9*, 4268−4272.

(5) Wofford, J. M.; Nie, S.; McCarty, K. F.; Bartelt, N. C.; Dubon, O. D. *Nano Lett.* **2010**, *10*, 4890−4896.

(6) Batzill, M. *Surf. Sci. Rep.* **2012**, *67*, 83−115.

(7) Losurdo, M.; Giangregorio, M. M.; Capezzuto, P.; Bruno, G. *J. Phys. Chem. C* **2011**, *115*, 21804−21812.

(8) Gao, L.; Guest, J. R.; Guisinger, N. P. *Nano Lett.* **2010**, *10*, 3512−3516.

(9) Rasool, H. I.; Song, E. B.; Mecklenburg, M.; Regan, B. C.; Wang, K. L.; Weiller, B. H.; Gimzewski, J. K. *J. Am. Chem. Soc.* **2011**, *133*, 12536−12543.

(10) Robinson, Z. R.; Tyagi, P.; Mowll, T. R.; Ventrice, C. A.; Hannon, J. B. *Phys. Rev. B* **2012**, *86*, 235413.

(11) Wilson, N.; Marsden, A.; Saghir, M.; Bromley, C.; Schaub, R.; Costantini, G.; White, T.; Partridge, C.; Barinov, A.; Dudin, P.; Sanchez, A.; Mudd, J.; Walker, M.; Bell, G. *Nano Res.* **2013**, *6*, 99−112.

(12) Murdock, A. T.; Koos, A.; Britton, T. B.; Houben, L.; Batten, T.; Zhang, T.; Wilkinson, A. J.; Dunin-Borkowski, R. E.; Lekka, C. E.; Grobert, N. *ACS Nano* **2013**, *7*, 1351−1359.

(13) Huang, P. Y.; Ruiz-Vargas, C. S.; van der Zande, A. M.; Whitney, W. S.; Levendorf, M. P.; Kevek, J. W.; Garg, S.; Alden, J. S.; Hustedt, C. J.; Zhu, Y.; Park, J.; McEuen, P. L.; Muller, D. A. *Nature* **2011**, *469*, 389−392.

(14) Ma, D.; Zhang, Y.; Liu, M.; Ji, Q.; Gao, T.; Zhang, Y.; Liu, Z. *Nano Res.* **2013**, *6*, 671−678.

(15) Chen, S.; Brown, L.; Levendorf, M.; Cai, W.; Ju, S.-Y.; Edgeworth, J.; Li, X.; Magnuson, C. W.; Velamakanni, A.; Piner, R. D.; Kang, J.; Park, J.; Ruoff, R. S. *ACS Nano* **2011**, *5*, 1321−1327.

(16) Schriver, M.; Regan, W.; Gannett, W. J.; Zaniewski, A. M.; Crommie, M. F.; Zettl, A. *ACS Nano* **2013**, *7*, 5763−5768.

(17) Wlasny, I.; Dabrowski, P.; Rogala, M.; Kowalczyk, P.; Pasternak, I.; Strupinski, W.; Baranowski, J.; Klusek, Z. *Appl. Phys. Lett.* **2013**, *102*, 111601−111601.

(18) Lu, A.-Y.; Wei, S.-Y.; Wu, C.-Y.; Hernandez, Y.; Chen, T.-Y.; Liu, T.-H.; Pao, C.-W.; Chen, F.-R.; Li, L.-J.; Juang, Z.-Y. *RSC Adv.* **2012**, *2*, 3008−3013.

(19) Zhou, F.; Li, Z.; Shenoy, G. J.; Li, L.; Liu, H. *ACS Nano* **2013**, *7*, 6939−6947.

(20) Rafiee, J.; Mi, X.; Gullapalli, H.; Thomas, A. V.; Yavari, F.; Shi, Y.; Ajayan, P. M.; Koratkar, N. A. *Nat. Mater.* **2012**, *11*, 217−222.

(21) Li, Z.; Wang, Y.; Kozbial, A.; Shenoy, G.; Zhou, F.; McGinley, R.; Ireland, P.; Morganstein, B.; Kunkel, A.; Surwade, S. P. *Nat. Mater.* **2013**, DOI: 10.1038/nmat3709.

(22) Raj, R.; Maroo, S. C.; Wang, E. N. *Nano Lett.* **2013**, *13*, 1509−1515.

(23) Malec, C. E.; Elkus, B.; Davidović, D. *Solid State Commun.* **2011**, *151*, 1791−1793.

(24) Liu, H.; Kondo, H.; Ohno, T. *Phys. Rev. B* **2012**, *86*, 155434.

(25) Dlubak, B.; Martin, M.-B.; Weatherup, R. S.; Yang, H.; Deranlot, C.; Blume, R.; Schloegl, R.; Fert, A.; Anane, A.; Hofmann, S. *ACS Nano* **2012**, *6*, 10930−10934.

(26) Nie, S.; Wofford, J. M.; Bartelt, N. C.; Dubon, O. D.; McCarty, K. F. *Phys. Rev. B* **2011**, *84*, 155425.

(27) Pirkle, A.; Chan, J.; Venugopal, A.; Hinojos, D.; Magnuson, C. W.; McDonnell, S.; Colombo, L.; Vogel, E. M.; Ruoff, R. S.; Wallace, R. M. *Appl. Phys. Lett.* **2011**, *99*, 122108−3.

(28) Walter, A. L.; Nie, S.; Bostwick, A.; Kim, K. S.; Moreschini, L.; Chang, Y. J.; Innocenti, D.; Horn, K.; McCarty, K. F.; Rotenberg, E. *Phys. Rev. B* **2011**, *84*, 195443.

(29) Marsden, A. J.; Asensio, M.; Avila, J.; Dudin, P.; Barinov, A.; Moras, P.; Sheverdyaeva, P. M.; White, T. W.; Maskery, I.; Costantini, G. *Phys. Status Solidi RRL-Rapid Res. Lett.* **2013**, *7*, 528−682.

(30) Khomyakov, P. A.; Giovannetti, G.; Rusu, P. C.; Brocks, G.; van den Brink, J.; Kelly, P. J. *Phys. Rev. B* **2009**, *79*, 195425.

(31) Giovannetti, G.; Khomyakov, P. A.; Brocks, G.; Karpan, V. M.; van den Brink, J.; Kelly, P. J. *Phys. Rev. Lett.* **2008**, *101*, 026803.

(32) Kong, L.; Bjelkevig, C.; Gaddam, S.; Zhou, M.; Lee, Y. H.; Han, G. H.; Jeong, H. K.; Wu, N.; Zhang, Z.; Xiao, J.; Dowben, P. A.; Kelber, J. A. *J. Phys. Chem. C* **2010**, *114*, 21618−21624.

(33) Rousseau, B.; Estrade-Szwarckopf, H. *Solid State Commun.* **2003**, *126*, 583−587.
(34) Puglia, C.; Bennich, P.; Hasselström, J.; Brühwiler, P. A.; Nilsson, A.; Li, Z. Y.; Rudolf, P.; Mårtensson, N. *Surf. Sci.* **2001**, *488*, 1−6.
(35) Wu, T.; Shen, H.; Sun, L.; Cheng, B.; Liu, B.; Shen, J. *ACS Appl. Mater. Interfaces* **2012**, *4*, 2041−2047.
(36) Zhang, L.; Ye, Y.; Cheng, D.; Pan, H.; Zhu, J. *J. Phys. Chem. C* **2013**, *117*, 9259−9265.
(37) Weatherup, R. S.; Bayer, B. C.; Blume, R.; Ducati, C.; Baehtz, C.; Schlögl, R.; Hofmann, S. *Nano Lett.* **2011**, *11*, 4154−4160.
(38) Weatherup, R. S.; Bayer, B. C.; Blume, R.; Baehtz, C.; Kidambi, P. R.; Fouquet, M.; Wirth, C. T.; Schlögl, R.; Hofmann, S. *ChemPhysChem* **2012**, *13*, 2544−2549.
(39) Tobin, J. P.; Hirschwald, W.; Cunningham, J. *Appl. Surf. Sci.* **1983**, *16*, 441−452.
(40) Panzner, G.; Egert, B.; Schmidt, H. P. *Surf. Sci.* **1985**, *151*, 400−408.
(41) Barr, T. L. *J. Phys. Chem.* **1978**, *82*, 1801−1810.
(42) Deroubaix, G.; Marcus, P. *Surf. Interface Anal.* **1992**, *18*, 39−46.
(43) Jin, S.; Atrens, A. *Appl. Phys.* **1987**, *42*, 149−165.
(44) Vlassiouk, I.; Regmi, M.; Fulvio, P.; Dai, S.; Datskos, P.; Eres, G.; Smirnov, S. *ACS Nano* **2011**, *5*, 6069−6076.
(45) Zhang, Y.; Li, Z.; Kim, P.; Zhang, L.; Zhou, C. *ACS Nano* **2011**, *6*, 126−132.
(46) Rasool, H. I.; Song, E. B.; Allen, M. J.; Wassei, J. K.; Kaner, R. B.; Wang, K. L.; Weiller, B. H.; Gimzewski, J. K. *Nano Lett.* **2010**, *11*, 251−256.
(47) Barinov, A.; Üstünel, H.; Fabris, S.; Gregoratti, L.; Aballe, L.; Dudin, P.; Baroni, S.; Kiskinova, M. *Phys. Rev. Lett.* **2007**, *99*, 046803.
(48) Zebda, A.; Sabbah, H.; Ababou-Girard, S.; Solal, F.; Godet, C. *Appl. Surf. Sci.* **2008**, *254*, 4980−4991.
(49) Gelius, U.; Heden, P.; Hedman, J.; Lindberg, B.; Manne, R.; Nordberg, R.; Nordling, C.; Siegbahn, K. *Phys. Scr.* **1970**, *2*, 70.
(50) Siokou, A.; Ravani, F.; Karakalos, S.; Frank, O.; Kalbac, M.; Galiotis, C. *Appl. Surf. Sci.* **2011**, *257*, 9785−9790.
(51) Ghijsen, J.; Tjeng, L. H.; van Elp, J.; Eskes, H.; Westerink, J.; Sawatzky, G. A.; Czyzyk, M. T. *Phys. Rev. B* **1988**, *38*, 11322−11330.
(52) Andersson, K.; Ketteler, G.; Bluhm, H.; Yamamoto, S.; Ogasawara, H.; Pettersson, L. G. M.; Salmeron, M.; Nilsson, A. *J. Phys. Chem. C* **2007**, *111*, 14493−14499.
(53) Larciprete, R.; Ulstrup, S.; Lacovig, P.; Dalmiglio, M.; Bianchi, M.; Mazzola, F.; Hornekær, L.; Orlando, F.; Baraldi, A.; Hofmann, P.; Lizzit, S. *ACS Nano* **2012**, *6*, 9551−9558.
(54) Sutter, P.; Sadowski, J. T.; Sutter, E. A. *J. Am. Chem. Soc.* **2010**, *132*, 8175−8179.
(55) Grånäs, E.; Knudsen, J.; Schröder, U. A.; Gerber, T.; Busse, C.; Arman, M. A.; Schulte, K.; Andersen, J. N.; Michely, T. *ACS Nano* **2012**, *6*, 9951−9963.
(56) Sutter, P.; Albrecht, P.; Tong, X.; Sutter, E. *J. Phys. Chem. C* **2013**, *117*, 6320−6324.
(57) O'Hern, S. C.; Stewart, C. A.; Boutilier, M. S.; Idrobo, J.-C.; Bhaviripudi, S.; Das, S. K.; Kong, J.; Laoui, T.; Atieh, M.; Karnik, R. *ACS Nano* **2012**, *6*, 10130−10138.
(58) Jeon, I.; Yang, H.; Lee, S.-H.; Heo, J.; Seo, D. H.; Shin, J.; Chung, U.-I.; Kim, Z. G.; Chung, H.-J.; Seo, S. *ACS Nano* **2011**, *5*, 1915−1920.
(59) Besenbacher, F.; Nørskov, J. K. *Prog. Surf. Sci.* **1993**, *44*, 5−66.
(60) Liu, J.; Wu, J.; Edwards, C. M.; Berrie, C. L.; Moore, D.; Chen, Z.; Maroni, V. A.; Paranthaman, M. P.; Goyal, A. *Adv. Funct. Mater.* **2011**, *21*, 3868−3874.
(61) Zhou, H.; Yu, W. J.; Liu, L.; Cheng, R.; Chen, Y.; Huang, X.; Liu, Y.; Wang, Y.; Huang, Y.; Duan, X. *Nat. Commun.* **2013**, *4*, 1539.
(62) López, G. A.; Mittemeijer, E. J. *Scr. Mater.* **2004**, *51*, 1−5.
(63) McLellan, R. B. *Scr. Met.* **1969**, *3*, 389−391.
(64) Kim, H.; Mattevi, C.; Calvo, M. R.; Oberg, J. C.; Artiglia, L.; Agnoli, S.; Hirjibehedin, C. F.; Chhowalla, M.; Saiz, E. *ACS Nano* **2012**, *6*, 3614−3623.
(65) Riikonen, S.; Krasheninnikov, A.; Halonen, L.; Nieminen, R. *J. Phys. Chem. C* **2012**, *116*, 5802−5809.
(66) Li, Y.; Li, M.; Gu, T.; Bai, F.; Yu, Y.; Trevor, M.; Yu, Y. *Appl. Surf. Sci.* **2013**, *284*, 207−213.
(67) Weatherup, R. S.; Dlubak, B.; Hofmann, S. *ACS Nano* **2012**, *6*, 9996−10003.
(68) Wirth, C. T.; Bayer, B. C.; Gamalski, A. D.; Esconjauregui, S.; Weatherup, R. S.; Ducati, C.; Baehtz, C.; Robertson, J.; Hofmann, S. *Chem. Mater.* **2012**, *24*, 4633−4640.
(69) Lee, S.; Lee, K.; Zhong, Z. *Nano Lett.* **2010**, *10*, 4702−4707.
(70) Bluhm, H.; Hävecker, M.; Knop-Gericke, A.; Kiskinova, M.; Schlögl, R.; Salmeron, M. *MRS Bull.* **2007**, *32*, 1022−1030.
(71) Seah, M. *Surf. Interface Anal.* **1986**, *9*, 85−98.
(72) Shirley, D. A. *Phys. Rev. B* **1972**, *5*, 4709.
(73) Doniach, S.; Sunjic, M. *J. Phys. C: Solid State Phys.* **1970**, *3*, 285.